# The Stability of the Electron Strahl against the Oblique Fast-magnetosonic/Whistler Instability in the Inner Heliosphere

Seong-Yeop Jeong[1] , Joel B. Abraham[1] , Daniel Verscharen[1] , Laura Berčič[1] , David Stansby[1] , Georgios Nicolaou[1],
Christopher J. Owen[1] , Robert T. Wicks[2] , Andrew N. Fazakerley[1], Jeffersson A. Agudelo Rueda[1] , and Mayur Bakrania[1]
[1] Mullard Space Science Laboratory, University College London, Dorking, RH5 6NT, UK; s.jeong.17@ucl.ac.uk
[2] Northumbria University, Newcastle, NE1 8ST, UK

## Abstract

We analyze the micro-kinetic stability of the electron strahl in the solar wind depending on heliocentric distance. The oblique fast-magnetosonic/whistler (FM/W) instability has emerged in the literature as a key candidate mechanism for the effective scattering of the electron strahl into the electron halo population. Using data from the Parker Solar Probe (PSP) and Helios, we compare the measured strahl properties with the analytical thresholds for the oblique FM/W instability in the low- and high-$\beta_{\parallel c}$ regimes, where $\beta_{\parallel c}$ is the ratio of the core parallel thermal pressure to the magnetic pressure. Our PSP and Helios data show that the electron strahl is on average stable against the oblique FM/W instability in the inner heliosphere. Our analysis suggests that the instability, if at all, can only be excited sporadically and on short timescales. We discuss the caveats of our analysis and potential alternative explanations for the observed scattering of the electron strahl in the solar wind. Furthermore, we recommend the numerical evaluation of the stability of individual distributions in the future to account for any uncertainties in the validity of the analytical expressions for the instability thresholds.

## 1. Introduction

The solar wind plasma is continuously emitted from the Sun into interplanetary space (Parker 1958; Neugebauer & Snyder 1962). It expands quasispherically and forms the heliosphere. The electrons are the most abundant particle species and play an important role in the solar wind. They guarantee quasineutrality and provide the solar wind with a significant heat flux through nonthermal properties of the electron velocity distribution functions (VDFs; Marsch 2006). In addition, the electrons generate a global ambipolar electric field through their thermal pressure gradient (Jockers 1970; Lemaire & Scherer 1970, 1971; Pierrard et al. 1999; Scudder 2019; Berčič et al. 2021).

According to previous in-situ measurements of the electron VDF in the solar wind, multiple deviations from a Maxwellian equilibrium state often occur. The electron VDFs typically consist of three different electron populations: the core, the halo, and the strahl. The core, which accounts for over 90% of the electrons in the solar wind, has a relatively low energy ($\lesssim 50\,\mathrm{eV}$) compared to the other populations and is quasi-isotropic. The halo has a greater energy ($\gtrsim 50\,\mathrm{eV}$) than the core and is nearly isotropic as well (Štverák et al. 2008; Salem et al. 2022). Lastly, the electron VDF often shows an energetic and highly field-aligned beam population known as the strahl. The strahl carries most of the heat flux (Feldman et al. 1975; Pilipp et al. 1987b) and becomes faint at large heliocentric distances (Pilipp et al. 1987a; Štverák et al. 2009; Graham et al. 2017). The continuing transfer of electrons from the strahl population into the halo population with increasing distance suggests that a local scattering mechanism modifies the shape of the VDF.

This mechanism is very important for the definition of the electron heat flux; however, its nature is still unknown.

Electron measurements in the solar wind provide evidence that fast-magnetosonic/whistler (FM/W) waves exchange energy with the electron strahl, which makes them a candidate to explain the scattering of the strahl into the halo population (Pagel et al. 2007; Lacombe et al. 2014; Graham et al. 2017). Linear theory suggests that the FM/W wave propagating in the antisunward direction with an oblique wavevector with respect to the background magnetic field can be driven unstable by the strahl through the anomalous cyclotron resonance and scatter strahl electrons in pitch angle through velocity space (Vasko et al. 2019; Verscharen et al. 2019). This strahl-driven instability has recently received a significant amount of attention in the literature as a local strahl scattering mechanism. Linear and quasilinear theories as well as numerical particle-in-cell (PIC) simulations support this picture (López et al. 2020; Jeong et al. 2020; Micera et al. 2020, 2021; Sun et al. 2021).

As the solar wind begins its journey in the corona where Coulomb collisions are more frequent than in the heliosphere, we anticipate that the core–halo–strahl configuration develops outside the corona. It is unknown at which heliocentric distance the local strahl scattering sets in. Based on a linear stability analysis, Horaites et al. (2018a) and Schroeder et al. (2021) argue against the action of a strahl-driven instability in the inner heliosphere at all. Parker Solar Probe (PSP) data from encounters 4 and 5 suggest that the strahl, at times, drives the oblique FM/W wave unstable at heliocentric distances below $54 r_s$ (Halekas et al. 2021), where $r_s$ is the solar radius. A kinetic expansion model for the solar wind electrons suggests, however, that the oblique FM/W instability is unlikely to occur regularly and scatter the electron strahl at heliocentric distances below $20 r_s$ (Jeong et al. 2022). Moreover, whistler waves are barely detected by PSP within $28 r_s$ (Cattell et al. 2022), supporting the notion that strahl scattering by the oblique FM/W instability is not a universal—or even

common—process in the inner heliosphere. We note, however, that the required whistler-wave amplitude for effective strahl scattering is small (Jeong et al. 2020; Vasko et al. 2020) and thus could be hidden in the fluctuation spectrum of the background turbulence in the solar wind (Zank et al. 1996; Chen et al. 2013; Tong et al. 2019).

In the present paper, we use the analytical thresholds for the oblique FM/W instability derived by Verscharen et al. (2019) to investigate the stability of the electron strahl in the inner heliosphere. By using PSP and Helios data, we quantify the analytical thresholds as functions of heliocentric distance. Our results show that, on average, the electron strahl is not scattered by the oblique FM/W instability in the inner heliosphere.

## 2. Methods

### 2.1. Thresholds for the Oblique FM/W Instability

To analyze the strahl scattering through the oblique FM/W instability, we evaluate the analytical thresholds in the low- and high-$\beta_{\parallel c}$ regimes provided by Verscharen et al. (2019). These analytical equations have been tested against numerical solutions for the thresholds of the oblique FM/W instability from linear hot-plasma theory over a range of representative solar wind parameters. The transition between the low-$\beta_{\parallel c}$ and high-$\beta_{\parallel c}$ regimes occurs at

$$\beta_{\parallel c} \approx 0.25, \tag{1}$$

where $\beta_{\parallel j} \equiv 8\pi n_j k_B T_{\parallel j}/B_0^2$, $n_j$ is the density of population $j$, $T_{\parallel j}$ is the temperature of population $j$ parallel to the background magnetic field, $B_0$ is the background magnetic field, and $k_B$ is the Boltzmann constant. The subscripts $e$, $c$, and $s$ indicate quantities related to the total electrons, the core and the strahl, respectively. The plasma crosses the analytical threshold of the oblique FM/W instability in the low-$\beta_{\parallel c}$ regime if

$$U_s \gtrsim 3v_{\parallel \mathrm{th},c}, \tag{2}$$

where $v_{\parallel \mathrm{th},c} = \sqrt{2k_B T_{\parallel c}/m_e}$ is the core parallel thermal speed, $U_s$ is the strahl bulk speed, and $m_e$ is the mass of an electron. The plasma crosses the analytical threshold of the oblique FM/W instability in the high-$\beta_{\parallel c}$ regime if

$$U_s \gtrsim \left[ 2\frac{n_s}{n_c}\sqrt{\frac{T_{\parallel s}}{T_{\parallel c}}} v_{Ae}^2 v_{\parallel \mathrm{th},c}^2 \frac{(1+\cos\theta)}{(1-\cos\theta)\cos\theta} \right]^{1/4}, \tag{3}$$

where $v_{Ae} = B_0/\sqrt{4\pi n_e m_e}$, and $\theta$ is the angle between wavevector $\boldsymbol{k}$ and $\boldsymbol{B}_0$.[3]

### 2.2. Data Analysis of PSP and Helios Data

We base our data analysis on the PSP data set created by Abraham et al. (2022). Our PSP data were recorded at heliocentric distances between $25r_s$ and $90r_s$. This data set uses fits to the observed level 3 electron VDFs provided by the Solar Wind Electron Alphas and Protons (SWEAP) instrument suite (Kasper et al. 2016; Whittlesey et al. 2020) on board PSP. SWEAP consists of two electrostatic analyzers, SPAN A and B, which measure electrons arriving from across almost the full sky using orthogonally positioned $120° \times 240°$ fields of

view over an energy range from 2 eV to 1793 eV during our measurement intervals. During the encounter, the sampling cadence of PSP's SPAN detector is 13.98 s, and its integration time is 6.965s. We fit the VDFs in the magnetic-field-aligned velocity frame and ignore any data points below 30 eV to avoid the inclusion of secondary electrons. The analysis method fits a bi-Maxwellian distribution to the core, a bi-$\kappa$-distribution to the halo, and a drifting bi-Maxwellian distribution to the strahl. We only allow the strahl to drift in the direction parallel to the magnetic field.

On Helios 1 and 2 (Rosenbauer et al. 1981; Pilipp et al. 1987a), electrons were measured by the electron particle instrument I2, part of the E1 Plasma Experiment. Our Helios data were recorded at heliocentric distances between $62r_s$ and $210r_s$. A narrow instrument aperture ($19° \times 2°$) spins with the spacecraft and covers a full range of $360°$ in azimuth, providing two-dimensional electron VDFs. Helios took 16 s to measure a full two-dimensional electron VDF with a cadence of 40 s. For context, we also use proton density and velocity as well as magnetic-field measurements as described by Berčič et al. (2019, Section 3). We analyze the electron VDFs in the magnetic-field-aligned frame, in which the solar-wind protons have zero bulk speed. We model the distributions with a sum of a bi-Maxwellian distribution representing the core, a bi-$\kappa$-distribution representing the halo, and a bi-Maxwellian distribution representing the strahl. We only allow the core and the strahl to have drift velocities in the direction parallel to the magnetic field.

In both data sets, we discard all VDFs for which the fit results for the density of the halo or the strahl is greater than the density of the core.

## 3. Results

### 3.1. Fit Parameters from PSP and Helios

We bin the fitted data from both PSP and Helios into 50 radial-distance bins of equal width. We first separate our PSP and Helios data into the low-$\beta_{\parallel c}$ regime and high-$\beta_{\parallel c}$ regime according to Equation (1). We show the profiles of $T_{\parallel c}$, $T_{\parallel s}$, $B_0$, $n_c/n_e$, $n_s/n_e$, and $v_{Ae}$, which all appear on the right-hand sides of Equations (2) and (3), as functions of heliocentric distance in Figure 1.

The red and blue lines correspond to the parameters in the low-$\beta_{\parallel c}$ regime while the yellow and green lines correspond to the parameters in the high-$\beta_{\parallel c}$ regime from PSP and Helios.

PSP predominately samples streams of slow solar wind while the Helios data set includes a broader variety of solar wind. Therefore, the PSP and Helios data sets do not connect exactly, especially in terms of $T_{\parallel s}$, $n_c/n_e$, and $n_s/n_e$ in the low-$\beta_{\parallel c}$ cases. Figure 1(c) shows the magnetic field averaged over the respective particle sampling times of the electron instruments for PSP and Helios.

For our evaluation of the instability thresholds as functions of heliocentric distance, we apply the binned mean profiles of the parameters shown in Figure 1 to Equations (2) and (3).

### 3.2. Threshold in the Low-$\beta_{\parallel c}$ Regime

In Figure 2, the blue (PSP) and red (Helios) lines show the profiles of the right-hand side of Equation (2), and the yellow (PSP) and green (Helios) lines show the measured profiles of $U_s$. The strahl bulk speed does not cross the low-$\beta_{\parallel c}$ threshold in the shown range of heliocentric distances on average and,

---

[3] The original derivation of the instability thresholds by Verscharen et al. (2019) assumes isotropic electrons. However, it is straightforward to extend this framework to anisotropic electrons, in which case we retrieve Equations (2) and (3).
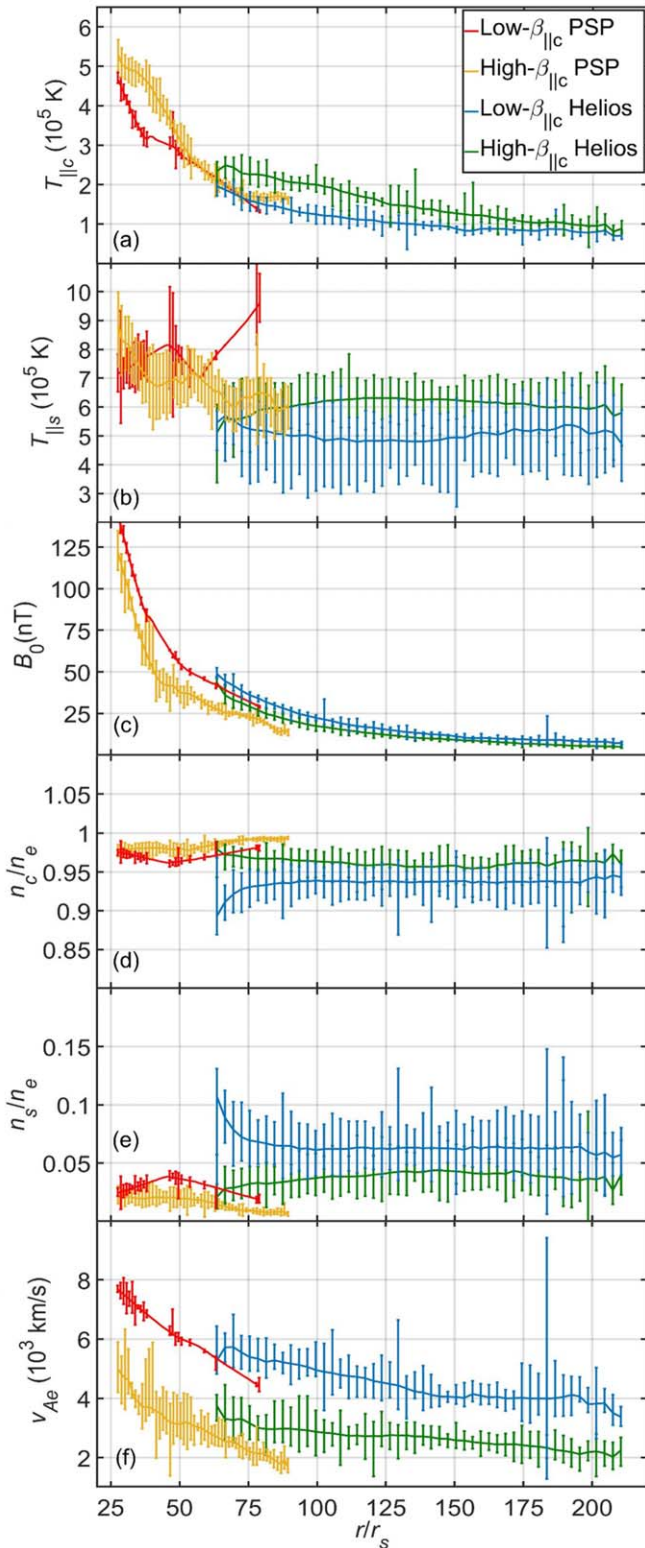
**Figure 1.** Radial profiles of $T_{\|c}$, $T_{\|s}$, $B_0$, $n_c/n_e$, $n_s/n_e$, and $v_{Ae}$ in our PSP and Helios data sets, separated between the low-$\beta_{\|c}$ and the high-$\beta_{\|c}$ regimes according to Equation (1).
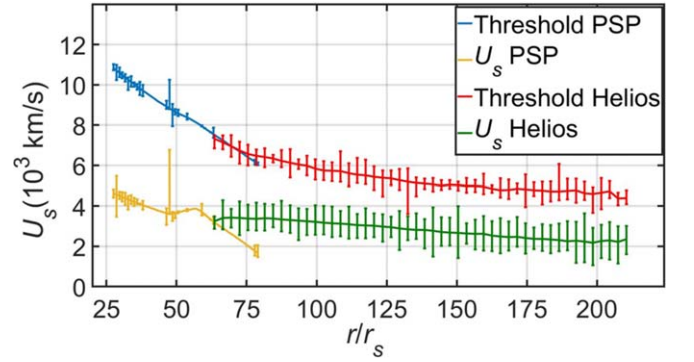


**Figure 2.** Profiles of the low-$\beta_{\|c}$ threshold of the oblique FM/W instability from Equation (2) and $U_s$ as functions of heliocentric distance. All PSP and Helios data underlying this figure have $\beta_{\|c} < 0.25$.



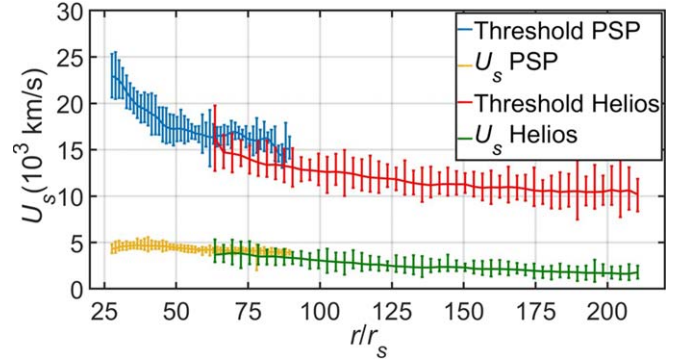**Figure 3.** Profiles of the high-$\beta_{\|c}$ threshold of the oblique FM/W instability from Equation (3) and $U_s$ as functions of heliocentric distance. All PSP and Helios data underlying this figure have $\beta_{\|c} > 0.25$.

threshold and $U_s$ do not overlap in the shown range of heliocentric distances.

### 3.3. Threshold in the High-$\beta_{\|c}$ Regime

Previous studies of the oblique FM/W instability by Vasko et al. (2019), Verscharen et al. (2019), López et al. (2020), Jeong et al. (2020), Micera et al. (2020), Micera et al. (2021), and Sun et al. (2021) suggest that the angle $\theta$ in Equation (3) typically ranges from $\theta = 55°$ to $65°$. Equation (3) does not significantly depend on $\theta$ in this range compared to its much stronger dependence on $T_{\|c}$, $T_{\|s}$, $n_c$, $n_s$, and $v_{Ae}$. Therefore, we use a representative value of $\theta = 60°$.

In Figure 3, the blue (PSP) and red (Helios) lines show the profiles of the right-hand side of Equation (3), and the yellow (PSP) and green (Helios) lines show the measured profile of $U_s$. The strahl bulk speed does not cross the high-$\beta_{\|c}$ threshold in the shown range of heliocentric distances on average and, thus, does not fulfill Equation (3). The high-$\beta_{\|c}$ threshold and $U_s$ quasi-monotonously decrease at all explored heliocentric distances. As in the low-$\beta_{\|c}$ case, near the Sun, the difference between the high-$\beta_{\|c}$ threshold and $U_s$ decreases with heliocentric distance. However, beyond $\sim 80 r_s$ from the Sun, the difference is approximately constant. The error bars of the high-$\beta_{\|c}$ threshold and $U_s$ do not overlap at all explored heliocentric distances.

### 4. Discussion and Conclusions

We analyze the stability of the solar-wind electron strahl against the oblique FM/W instability for self-induced strahl

thus, does not fulfill Equation (2). The low-$\beta_{\|c}$ threshold and $U_s$ decrease quasi-monotonously. Near the Sun, the difference between the low-$\beta_{\|c}$ threshold and $U_s$ decreases with heliocentric distance. However, beyond $\sim 80 r_s$ from the Sun, the difference is nearly constant. The error bars of the low-$\beta_{\|c}$

scattering in two different $\beta_{\parallel c}$ regimes. By quantifying the plasma parameters based on binned and averaged electron data from PSP and Helios, as shown in Figure 1, we evaluate the analytical instability thresholds as functions of heliocentric distance.

Our results show that Equations (2) and (3) are, for plasma with the observed average radial profiles, not satisfied at heliocentric distances between $25r_s$ and $210r_s$. In Figures 2 and 3, the low- and high-$\beta_{\parallel c}$ thresholds are always greater than $U_s$. For both the low-$\beta_{\parallel c}$ and for the high-$\beta_{\parallel c}$ cases, the difference between the thresholds and $U_s$ decreases with heliocentric distance near the Sun as predicted by Jeong et al. (2022, section 4.4). However, beyond a heliocentric distance of $\sim 80r_s$, the difference between the thresholds and $U_s$ is nearly constant. Assuming that our PSP and Helios data are representative and that our Equations (2) and (3) reflect the thresholds accurately, our findings suggest that the strahl is not scattered by the oblique FM/W instability in the inner heliosphere, in agreement with the arguments presented by Horaites et al. (2018a) and Schroeder et al. (2021).

According to quasilinear theory and particle-in-cell simulations (Jeong et al. 2020; Micera et al. 2020, 2021), the oblique FM/W instability, if excited, scatters the electron strahl efficiently on a timescale shorter than 1 s in the inner heliosphere. This rapid action of the instability and the radial decrease of the thresholds suggest that the measured $U_s$ would closely follow the threshold of marginal stability at all distances beyond the critical distance $r_{\rm crit}$, at which the threshold is crossed for the first time. Neither Figure 2 nor Figure 3 suggests the existence of $r_{\rm crit}$ at heliocentric distances less than 1 au. However, we identify some uncertainties in our results.

Our analysis is based on electron measurements with a finite sampling cadence ($\sim 14$ s by PSP and $\sim 40$ s by Helios). Even if the instability scatters the electron strahl, PSP and Helios would be unlikely to detect the moment of strahl scattering because it occurs so quickly. If the magnetic field changes significantly during such a sampling interval, the corresponding electron measurement would be deteriorated. Since the averaged amplitude of magnetic-field variations at the timescale of the particle measurements is small, we assume that this effect has a small impact on our results. However, we recommend repeating our study with even faster plasma instrumentation (e.g., with Solar Orbiter's EAS instrument in burst mode, Owen et al. 2020) for comparison in the future.

The derivation of Equations (2) and (3) by Verscharen et al. (2019) is based on the assumption that the oblique FM/W instability is most efficiently driven by electrons with $v_{\parallel} = U_s$, where $v_{\parallel}$ is the velocity coordinate in the direction parallel with respect to $\vec{B}_0$ in the solar wind frame. However, according to the predictions from quasilinear theory and PIC simulations (Jeong et al. 2020; Micera et al. 2020, 2021), strahl scattering by the oblique FM/W instability most efficiently occurs in the $v_{\parallel}$-range $\gtrsim U_s$. For example, Jeong et al. (2020) show that the oblique FM/W instability in the high-$\beta_{\parallel c}$ regime is most efficiently driven by electrons with $v_{\parallel} \approx 2U_s$. Applying this argument in the derivation of Equation (3), we find a threshold for the high-$\beta_{\parallel c}$ case that is lower by a factor of about two than shown in Figure 3. Such a modification would lead to a small difference between the two curves shown in Figure 3. If we adjusted the analytical thresholds by a constant factor greater than 2, the discovered constant difference between the thresholds and $U_s$ at $r \gtrsim 80r_s$ would be consistent with the limitation of $U_s$ through the oblique FM/W instability with $r_{\rm crit} \approx 80r_s$.

The uncertainties of the analytical instability thresholds can be circumvented by calculating the stability of individually measured electron VDFs with numerical tools like ALPS (Verscharen et al. 2018) or LEOPARD (Astfalk & Jenko 2017). These numerical codes are able to calculate the full hot-plasma dispersion relation based on our PSP and Helios data without assuming a bi-Maxwellian shape of the electron VDF. This method would allow for an independent determination of $r_{\rm crit}$ and thus an independent determination of a potential correction factor to our analytical instability thresholds. In addition, it would be worthwhile to investigate observationally the occurrence of oblique FM/W waves as a result of the oblique FM/W instability.

Our observation of the decreasing trends in $U_s$ (Figures 2 and 3) as well as earlier observations of the broadening of the strahl pitch angle and the scattering of the strahl into the halo (Hammond et al. 1996; Maksimovic et al. 2005; Štverák et al. 2009; Graham et al. 2017) provide evidence that strahl scattering occurs over a wide range of distances in the solar wind. Therefore, if the oblique FM/W instability is *not* responsible for this evolution, other processes must explain the observed trends.

Other linear instabilities, including the quasiparallel whistler heat-flux instability (Tong et al. 2019; Kuzichev et al. 2019; Vasko et al. 2020) are not efficient strahl scattering mechanisms (Verscharen et al. 2019). However, nonlinear processes involving combinations of primary and secondary instabilities in connection with solar wind expansion reproduce observed wave and particle features in the solar wind (Micera et al. 2021). Coulomb collisions have been suggested to contribute to the strahl evolution even though the collisional mean free path of suprathermal electrons is large (Landi et al. 2012; Horaites et al. 2018b, 2019). Another possible strahl scattering mechanism involves the dissipation of existing plasma fluctuations (especially whistler waves; Vocks 2012; Vocks et al. 2005). Although whistler waves have been sporadically observed in the solar wind (Lacombe et al. 2014; Agapitov et al. 2020; Kretzschmar et al. 2021; Cattell et al. 2021; Jagarlamudi et al. 2021), their origin and possible links to solar wind turbulence are still not well understood.

## ORCID iDs

Seong-Yeop Jeong ⓘ https://orcid.org/0000-0001-8529-3217
Joel B. Abraham ⓘ https://orcid.org/0000-0002-6305-3252
Daniel Verscharen ⓘ https://orcid.org/0000-0002-0497-1096

Laura Berčič https://orcid.org/0000-0002-6075-1813
David Stansby https://orcid.org/0000-0002-1365-1908
Christopher J. Owen https://orcid.org/0000-0002-5982-4667
Robert T. Wicks https://orcid.org/0000-0002-0622-5302
Jeffersson A. Agudelo Rueda https://orcid.org/0000-0001-5045-0323
Mayur Bakrania https://orcid.org/0000-0001-6225-9163

## References

Abraham, J. B., Owen, C. J., Verscharen, D., et al. 2022, ApJ, submitted
Agapitov, O. V., de Wit, T. D., Mozer, F. S., et al. 2020, ApJ, 891, L20
Astfalk, P., & Jenko, F. 2017, JGRA, 122, 89
Berčič, L., Maksimović, M., Halekas, J. S., et al. 2021, ApJ, 921, 83
Berčič, L., Maksimović, M., Landi, S., & Matteini, L. 2019, MNRAS, 486, 3404
Cattell, C., Breneman, A., Dombeck, J., et al. 2022, ApJL, 924, L33
Cattell, C., Short, B., Breneman, A., et al. 2021, A&A, 650, A8
Chen, C. H. K., Boldyrev, S., Xia, Q., & Perez, J. C. 2013, PhRvL, 110, 225002
Feldman, W. C., Asbridge, J. R., Bame, S. J., Montgomery, M. D., & Gary, S. P. 1975, JGR, 80, 4181
Graham, G. A., Rae, I. J., Owen, C. J., et al. 2017, JGRA, 122, 3858
Halekas, J. S., Whittlesey, P. L., Larson, D. E., et al. 2021, A&A, 650, A15
Hammond, C. M., Feldman, W. C., McComas, D. J., Phillips, J. L., & Forsyth, R. J. 1996, A&A, 316, 350
Horaites, K., Astfalk, P., Boldyrev, S., & Jenko, F. 2018a, MNRAS, 480, 1499
Horaites, K., Boldyrev, S., & Medvedev, M. V. 2019, MNRAS, 484, 2474
Horaites, K., Boldyrev, S., Wilson, Lynn B., I., Viñas, A. F., & Merka, J. 2018b, MNRAS, 474, 115
Jagarlamudi, V. K., Dudok de Wit, T., Froment, C., et al. 2021, A&A, 650, A9
Jeong, S.-Y., Verscharen, D., Wicks, R. T., & Fazakerley, A. N. 2020, ApJ, 902, 128
Jeong, S.-Y., Verscharen, D., Vocks, C., et al. 2022, ApJ, in press (arXiv:2201.00079)
Jockers, K. 1970, A&A, 6, 219
Kasper, J. C., Abiad, R., Austin, G., et al. 2016, SSRv, 204, 131
Kretzschmar, M., Chust, T., Krasnoselskikh, V., et al. 2021, A&A, 656, A24
Kuzichev, I. V., Vasko, I. Y., Soto-Chavez, A. R., et al. 2019, ApJ, 882, 81
Lacombe, C., Alexandrova, O., Matteini, L., et al. 2014, ApJ, 796, 5
Landi, S., Matteini, L., & Pantellini, F. 2012, ApJ, 760, 143
Lemaire, J., & Scherer, M. 1970, P&SS, 18, 103
Lemaire, J., & Scherer, M. 1971, JGR, 76, 7479
López, R. A., Lazar, M., Shaaban, S. M., Poedts, S., & Moya, P. S. 2020, ApJ, 900, L25
Maksimovic, M., Zouganelis, I., Chaufray, J.-Y., et al. 2005, JGRA, 110, A09104
Marsch, E. 2006, LRSP, 3, 1
Micera, A., Zhukov, A. N., López, R. A., et al. 2021, ApJ, 919, 42
Micera, A., Zhukov, A. N., López, R. A., et al. 2020, ApJ, 903, L23
Neugebauer, M., & Snyder, C. W. 1962, Sci, 138, 1095
Owen, C. J., Bruno, R., Livi, S., et al. 2020, A&A, 642, A16
Pagel, C., Gary, S. P., de Koning, C. A., Skoug, R. M., & Steinberg, J. T. 2007, JGRA, 112, A04103
Parker, E. N. 1958, ApJ, 128, 664
Pierrard, V., Maksimovic, M., & Lemaire, J. 1999, JGRA, 104, 17021
Pilipp, W. G., Miggenrieder, H., Montgomery, M. D., et al. 1987a, JGRA, 92, 1075
Pilipp, W. G., Miggenrieder, H., Mühlhäuser, K. H., et al. 1987b, JGRA, 92, 1103
Rosenbauer, H., Schwenn, R., Miggenrieder, H., et al. 1981, The instruments of the plasma experiment onboard the HELIOS solar probe, Max-Planck-Inst. für Aeronomie, Katlenburg-Lindau
Salem, C. S., Pulupa, M., Bale, S. D., & Verscharen, D. 2022, A&A, in press (arXiv:2107.08125)
Schroeder, J. M., Boldyrev, S., & Astfalk, P. 2021, MNRAS, 507, 1329
Scudder, J. D. 2019, ApJ, 882, 146
Štverák, Š., Maksimovic, M., Trávníček, P. M., et al. 2009, JGRA, 114, A05104
Štverák, Š., Trávníček, P. M., Maksimovic, M., et al. 2008, JGRA, 113, A03103
Sun, H., Zhao, J., Liu, W., et al. 2021, ApJL, 916, L4
Tong, Y., Vasko, I. Y., Artemyev, A. V., Bale, S. D., & Mozer, F. S. 2019, ApJ, 878, 41
Vasko, I. Y., Krasnoselskikh, V., Tong, Y., et al. 2019, ApJL, 871, L29
Vasko, I. Y., Kuzichev, I. V., Artemyev, A. V., et al. 2020, PhPl, 27, 082902
Verscharen, D., Klein, K. G., Chandran, B. D. G., Stevens, M. L., Salem, C. S., & Bale, S. D. 2018, JPlPh, 84, 905840403
Verscharen, D., Chandran, B. D. G., Jeong, S.-Y., et al. 2019, ApJ, 886, 136
Vocks, C. 2012, SSRv, 172, 303
Vocks, C., Salem, C., Lin, R. P., & Mann, G. 2005, ApJ, 627, 540
Whittlesey, P. L., Larson, D. E., Kasper, J. C., et al. 2020, ApJS, 246, 74
Zank, G. P., Matthaeus, W. H., & Smith, C. W. 1996, JGRA, 101, 17093